

## Magneto-flow instability in symmetric field profiles

T. Tatsuno<sup>a)</sup> and W. Dorland

*Center for Scientific Computation and Mathematical Modeling, The University of Maryland, College Park, Maryland 20742-3289*

(Received 26 June 2006; accepted 28 July 2006; published online 12 September 2006)

Since Rayleigh's early work on shear-flow driven instabilities in fluids, it has been known that sheared flows are usually unstable only in the presence of an inflection point in the velocity profile. However, in magnetohydrodynamics, there are important instabilities for which no inflection point is required. In tokamak experiments, strongly sheared flows are associated with transport barriers. Instabilities that may limit the height and extent of transport barriers are of central importance. Here, we present linear and nonlinear simulations of an ideal magnetohydrodynamic instability that is driven by sheared flows without inflection points—instead, the instability mechanism requires reversed magnetic shear. Several symmetric field profiles are studied. In general, the instability leads to current profile modifications that push the local minimum value of the safety factor ( $q_{\min}$ ) upward. The possibility of causing disruption in a relatively slow time scale is pointed out when  $q_{\min}$  crosses a rational (especially integral) value. The time scale of the instability is governed by the transit time of the shear flow, which is typically smaller than that of the Alfvén velocity. Characteristics of this instability are compared with recent experimental observations.

© 2006 American Institute of Physics. [DOI: [10.1063/1.2338819](https://doi.org/10.1063/1.2338819)]

### I. INTRODUCTION

Shear flow instability in plasmas is a profound problem that has rich consequences and is not understood well. Shear flow appears in almost all laboratory or astrophysical situations, from tokamaks to active galactic nuclei. The most well-known instability incurred by shear flow is the Kelvin-Helmholtz (KH) instability. The KH instability is associated an inflection point in the velocity profile, and occurs even without a magnetic field.<sup>1</sup> An investigation of this instability in plasma, including the effect of the ambient magnetic field, drift and/or gyromotion, is an area of active research.<sup>2</sup>

The KH instability is not the only instability driven by sheared flow in magnetized plasma. It is known that the combination of stable shear flow and an inhomogeneous magnetic field can lead to another ideal magnetohydrodynamic (MHD) instability.<sup>3–5</sup> In the case of unmagnetized plane Couette flow, the isosurface of the perturbed vorticity is stretched away by the background shear flow since perturbed vorticity is conserved. However, Stern<sup>3</sup> first realized that just as the inflection point in the KH instability breaks this constraint,<sup>1</sup> an inhomogeneous magnetic field can have a similar effect, and lead to instability. Kent<sup>4</sup> has extended this idea to the case of a symmetric flow profile, and obtained several instability conditions in terms of the equilibrium values at the boundary of the domain. Chen and Morrison<sup>5</sup> revisited Kent's work and found a profile as simple as linear flow and a parabolic field. We will refer frequently to this simplest case in the present paper.

Previous authors have treated the problem with analytic methods such as perturbation theory and Nyquist analyses. They only have obtained the marginal stability condition, and the growth rate has never been given as a function of the

wavenumber. In this paper, we focus on the single-fluid MHD equations, take the linear shear flow profile which is KH stable, and investigate the effect of various profiles of the magnetic field in slab geometry. Our approach is primarily numerical. Note that the linear flow profile is itself stable without a magnetic field, and any magnetic field profile is ideally stable in slab geometry without background flow, so this instability is truly a combined effect of shear flow and magnetic field.

The reader might think that magnetorotational instability (MRI) is one of the other cases where the stable shear flow could be destabilized by the inclusion of a weak magnetic field.<sup>6</sup> However, unlike this instability, MRI has an intrinsic drive (centrifugal force) other than shear flow itself and the physics of its nonaxisymmetric perturbation would be closer to that reported in Ref. 7, which investigates the effect of shear flow on the plasma with an interchange drive: Shear-flow stabilized interchange could reappear when one adds a magnetic field. Similarly, the so-called “joint instability” is investigated in the context of solar physics<sup>8</sup> as an extension of the aforementioned works, where it was found that the combination of stable shear flow and an inhomogeneous magnetic field could cause MHD instability. However, the effect of the curvature makes the problem complicated since their investigation focuses on the spherical geometry.

Experimentally, an intermediate time-scale instability was recently observed in the reversed shear discharges of JT-60U,<sup>9</sup> where the growth rate was found to be small compared to an ideal instability but too large for a resistive one. In more recent experiments,<sup>10,11</sup> a considerable amount of flow is often observed, which has a strong shear around the internal transport barrier. Here, we consider a field profile that may be relevant to these observations. The inferred flow profiles might contain inflection points. Our aim is to explore

<sup>a)</sup>Electronic mail: tatsuno@umd.edu

the magneto-flow instability, which could limit performance even in the absence of an inflection point. More detailed comparisons will be required to determine which instabilities are in fact dominant. The growth rate of this instability is governed by the shear flow. It is larger than that of the typical resistive instability and smaller than that of the typical magnetic-field driven ideal instability. Therefore, we believe that it is important to investigate this instability carefully, albeit in the simplest slab geometry.

We present our formulation and the general properties of the linear eigenvalue equation in Sec. II. Since the instability is global and depends strongly on the details of the field profile (we focus on a linear flow profile) it is difficult to make a quantitative discussion by analytic calculation. We cannot discuss the instability in the infinite domain, since the infinite difference of the shear flow at both edges prevents any exponential instability to grow due to its stretching (shearing) effect.<sup>12,13</sup> On the other hand, a study of this instability in a periodic domain would inevitably introduce inflection points, which makes it difficult to distinguish the phenomena from KH instability.<sup>14</sup> In practice, the overall dispersion relation has never been obtained by analytic calculation, even in the simplest slab geometry. In light of these difficulties, we decided to pursue mainly numerical analyses, which we report here.

Several numerical solutions of the linear eigenvalue equation are obtained by invoking the shooting code, and are shown in Sec. III. These analyses reveal the general conditions that maximize the growth rate: (a) the phase velocity of the Alfvén wave *in the direction of* the background mass velocity around the edge region should have comparable, but smaller, values than the local mass flow, (b) the central value of  $\mathbf{k} \cdot \mathbf{B}$  should be finite and have different sign from both edges, and thus, (c)  $\mathbf{k} \cdot \mathbf{B}$  should change sign twice in the domain, where  $\mathbf{k}$  denotes the wavenumber in the homogeneous direction. These basic features lead one to suspect that the  $q_{\min}$  surface of an advanced tokamak may be susceptible to this instability. We show a concrete example of a profile that may be applicable to this situation.

Results from nonlinear simulations are presented in Sec. IV. In order to simulate the incompressible motion of the plasma, we developed a pseudospectral code that solves two-dimensional reduced MHD equations, in a vorticity-streamfunction and flux function formulation. The nonperiodicity of the problem leads to the choice of Chebyshev polynomials for the basis functions. The Chebyshev spectral scheme is nowadays a common tool to solve fluid dynamical turbulence problems, including boundaries. However, it is not as popular in plasma physics as it is in fluid mechanics. The development of the combined reduced MHD-Chebyshev formulation presented here may have wider applications, and is therefore presented in some detail. In the specific case studied here, we find that nonlinear evolution of the above mentioned tokamak example may lead to disruption with a time scale slower than Alfvén time and faster than the resistive one, which might account for the disruption recently observed in JT-60U.<sup>9</sup>

Finally, the summary is given in Sec. V.

## II. FORMULATION

We wish to consider incompressible plasma motion in slab geometry with equilibrium sheared flows. The governing equations are

$$\rho(\partial_t \mathbf{v} + \mathbf{v} \cdot \nabla \mathbf{v}) = \frac{1}{\mu_0} (\nabla \times \mathbf{B}) \times \mathbf{B} - \nabla p, \quad (1)$$

$$\partial_t \mathbf{B} - \nabla \times (\mathbf{v} \times \mathbf{B}) = 0, \quad (2)$$

$$\nabla \cdot \mathbf{v} = 0, \quad \text{and} \quad \nabla \cdot \mathbf{B} = 0, \quad (3)$$

where the density  $\rho$  is assumed constant.

Dividing all fields into equilibrium and perturbed parts, the former (latter) is expressed by the uppercase (lowercase) letter in this and subsequent sections. We consider a general one-dimensional slab equilibrium, including both parallel and perpendicular shear flows. The magnetic field and flow profiles are given by

$$\mathbf{B} = [0, B_y(x), B_z(x)], \quad (4)$$

$$\mathbf{V} = [0, V_y(x), 0], \quad (5)$$

in Cartesian coordinates. The equilibrium pressure  $P(x)$  is chosen such that

$$\frac{d}{dx} \left( P + \frac{B^2}{2\mu_0} \right) = 0. \quad (6)$$

The profiles of equilibrium magnetic and velocity fields may be arbitrary functions of  $x$ . As we mentioned in Sec. I, we concentrate on the linear shear flow profile (plane Couette flow) in this paper. Since the infinite size of the domain in the  $x$  direction introduces the infinite difference of the background flow between both edges of the system,<sup>12,13</sup> we set our domain  $x \in [-L, L]$  and put a no-slip, ideal conducting wall at  $x = \pm L$ .

Upon linearizing the equation of motion, taking its curl, and assuming the *ansatz*

$$f(x, y, z, t) = f(x) \exp[i(k_y y + k_z z - \omega t)], \quad (7)$$

for all perturbed quantities, we obtain the eigenvalue ODE:

$$\frac{d}{dx} \left[ \left( \Omega^2 - \frac{F^2}{\mu_0 \rho} \right) \frac{d}{dx} \left( \frac{v_x}{\Omega} \right) \right] - (k_y^2 + k_z^2) \left( \Omega^2 - \frac{F^2}{\mu_0 \rho} \right) \frac{v_x}{\Omega} = 0, \quad (8)$$

where  $\Omega = \omega - \mathbf{k} \cdot \mathbf{V}$  and  $F = \mathbf{k} \cdot \mathbf{B}$ . The boundary condition introduced by the no-slip, ideal wall implies  $v_x = 0$  at  $x = \pm L$ .

It is convenient to normalize (8) by the half system size  $L$  and characteristic poloidal Alfvén velocity  $v_{pA}^*$ :  $= B_y^* / \sqrt{\mu_0 \rho}$ , where  $B_y^*$  is chosen such that  $B_y(x)$  is order unity:

$$x = L\hat{x}, \quad V_y = v_{pA}^* \hat{V}_y, \quad t = \frac{L}{v_{pA}^*} \hat{t}, \quad (9)$$

$$\omega = \frac{v_{pA}^*}{L} \hat{\omega}, \quad k = \frac{1}{L} \hat{k}, \quad \frac{d}{dx} = \frac{1}{L} \frac{d}{d\hat{x}}. \quad (10)$$

Here the values carrying  $\hat{\phantom{x}}$  denote the normalized variables. The normalized ODE is

$$\frac{d}{d\hat{x}} \left[ (\hat{\Omega}^2 - \hat{F}^2) \frac{d}{d\hat{x}} \left( \frac{\hat{v}_x}{\hat{\Omega}} \right) \right] - \hat{k}^2 (\hat{\Omega}^2 - \hat{F}^2) \frac{\hat{v}_x}{\hat{\Omega}} = 0, \quad (11)$$

where  $\hat{F} = \hat{k} \cdot \hat{\mathbf{B}}$  and  $\hat{k} = \sqrt{\hat{k}_y^2 + \hat{k}_z^2}$ . Hereafter, we omit the  $\hat{\phantom{x}}$  for the normalized quantities, and the values mean the normalized ones unless we explicitly mention otherwise.

We now summarize the general properties of the ODE (11).

If  $k_y=0$ , the effect of shear flow is excluded and the ODE (11) reduces to the one for static equilibria. Thus we know the system is stable, and we do not consider this case here.

Since the magnetic field appears only as a square in (11), the sign of  $B_y$  or  $B_z$  does not affect the instability.

If  $\omega = \omega_e$  is an eigenvalue for a certain velocity profile  $V_y = V_e(x)$ , then  $\omega = \omega_e + k_y V_0$  becomes an eigenvalue for the velocity profile  $V_y = V_0 + V_e(x)$  with the same eigenfunction, where  $V_0$  is a constant velocity, since these combinations yield the same factor,  $\Omega = \omega_e - k_y V_e$  (Doppler shift). Thus, we may assume  $V_y(0) = 0$  without loss of generality.

From the sufficient condition of stability given by several authors,<sup>3,15,16</sup> it is clear that the system is stable if there is a reference frame in which the local Alfvén velocity projected onto the mass flow direction is larger than the local flow velocity everywhere in the domain. That is, in physical units,

$$|V_y| \leq \left| \frac{k_{\parallel} v_A}{k_y} \right| (\nabla x), \quad (12)$$

where  $v_A = |\mathbf{B}| / \sqrt{\mu_0 \rho}$  so that  $k_{\parallel} v_A = F$ . The inverse may not be true. This means that the velocity  $V_y$  has to exceed the value of the Alfvén velocity (directed along  $\mathbf{B}$ ) projected onto the direction of  $V_y$ . Note that this condition does not necessarily mean that  $V_y$  has to be larger than the Alfvén velocity, defined by  $B_y$ . An example is given in Sec. III B. Another caveat of condition (12) is that it is not the magnitude of the flow itself but the flow shear that matters, as was seen in the previous paragraph. On the other hand, it is the magnitude of the magnetic field that matters and not the magnetic shear only. Thus it is sufficient for stability if the condition (12) is satisfied in a particular reference frame.

It is important to realize that the direction of shear flow does not need to be parallel to the ambient magnetic field. When a field profile yields instability for a parallel flow, then the same profile with perpendicular flow will also lead to instability if we may rescale the length. Since we derived a linearized ODE for the ambient field and flow (4) and (5), let us fix the flow profile with  $\mathbf{V} = [0, V_y(x), 0]$  and change the direction of field to check the effect of parallel/perpendicular flow with respect to the field. If one finds an instability for a parallel flow where  $\mathbf{B} = [0, B(x), 0]$  with a wavenumber  $(k_y, k_z) = (k_e, 0)$ , let its eigenvalue and eigenfunction be  $\omega_e$  and  $\varphi_e (=v_x/\Omega)$ . Then, the same field profile yields the instability for the wavenumber  $(k_y, k_z) = (k_e, k_e)/\sqrt{2}$  with an eigenvalue  $\omega = \omega_e/\sqrt{2}$  and eigenfunction  $\varphi_e$  in case of a perpendicular flow where  $\mathbf{B} = [0, 0, B(x)]$ . Thus we mainly concentrate on the parallel flow in this paper, except in Sec. III B, where we show an explicit example for the application

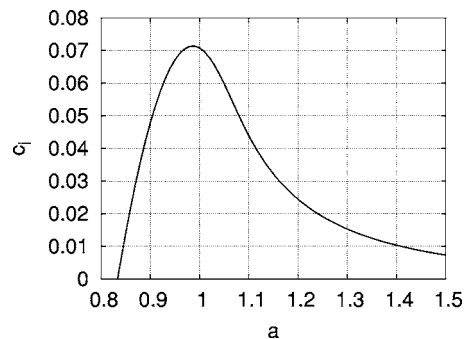


FIG. 1. Instability threshold and maximum  $c_i$  for parabolic field profile  $B_y = ax^2$ .

of a tokamak. We also note that the longitudinal magnetic field ( $B_z$ ) enters only through  $F$  and thus does not affect the mode at all as far as  $k_z = 0$ .

### III. LINEAR INSTABILITY

#### A. Parallel flow

As was obtained by Chen and Morrison,<sup>5</sup> we have plotted  $c_i (= \lim_{k_y \rightarrow 0} \omega_i/k_y)$  with respect to  $a$  in Fig. 1, where the flow profile is fixed at  $V_y(x) = x$  and a parallel magnetic field of the following form is assumed:

$$B_y(x) = ax^2. \quad (13)$$

In agreement with their analytical estimate, we find that the critical value above which the instability occurs is  $a \approx 0.834$ . As long as  $a > 0.834$ , the system is unstable. However, for larger values of  $a$  ( $a < 30$ ;  $c_i \geq 3.28 \times 10^{-8}$ ), our numerical results indicate that  $c_i$  converges to zero with  $c_i \approx 0.027a^{-4}$ . The dispersion relation is shown in Fig. 2 for  $a = 1$ , namely, for the almost largest  $c_i$ . The growth rate has a maximum at finite  $k_y$  ( $\approx 0.8$  in this case), and the instability is quenched for a larger  $k_y$ , which is similar to the behavior of KH instability. The real part of  $\omega$  may be finite, in general, but turned out to be zero for all  $k_y$  in the examples shown in this paper.

In the following sections, we discuss the property of this instability by showing the dependence of the growth rate on the various ambient field profiles.

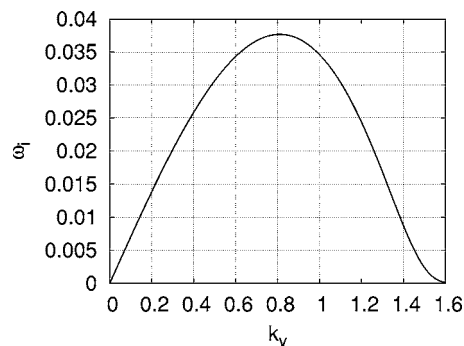


FIG. 2. Dispersion relation for  $V_y(x) = x$  and  $B_y(x) = x^2$ .

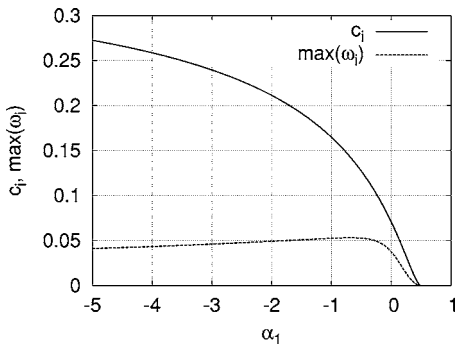


FIG. 3. The quantity  $c_i$  and  $\max_{k_y} \omega_i$  for the field profile  $B_y(x) = (1 - \alpha_1)x^2 + \alpha_1$ .

**1. Dependence on central value of field**

The instability remains when the magnetic field is modified to

$$B_y = (1 - \alpha_1)x^2 + \alpha_1, \tag{14}$$

which changes the value of  $B_y(0) = \alpha_1$  with  $B_y(\pm 1) = 1$  fixed. The maximum growth rate  $\max_{k_y}(\omega_i)$  and the quantity  $c_i$  are plotted with respect to  $\alpha_1$  in Fig. 3. Here the upper bound of  $\alpha_1 \approx 0.5$  for instability comes from the fact that local Alfvén velocity exceeds the local flow velocity everywhere in the domain, which corresponds to (12). For negative  $\alpha_1$ , we have larger  $c_i$ , as we see from Fig. 3. For  $\alpha_1 \geq -25$ , we find no maximum of  $c_i$  with respect to  $\alpha_1$ . As we decrease  $\alpha_1$ , however, the upper bound of  $k_y$  for instability decreases while the  $c_i$  corresponding to  $\omega_i/k_y$  in the limit  $k_y \rightarrow 0$  increases. With the combined effect of them, the maximum growth rate is achieved at about  $\alpha_1 \approx -0.7$  for  $k_y \approx 0.6$ .

**2. Dependence on edge shear**

Chen and Morrison<sup>5</sup> mention in their paper that the “magnetic field at the boundaries tends to destabilize the shear flow.” This is certainly true for the analytically tractable case where  $B_y(x)$  is parabolic. To check the statement for general profiles of  $B_y$ , we prepared a profile,

$$B_y = 1 - \frac{\tanh^2 \alpha_2 x}{\alpha_2^2 x^2}, \tag{15}$$

to compare with the parabolic one. This profile is shown for  $\alpha_2 = 2$  in Fig. 4, where the dotted line shows the profile of

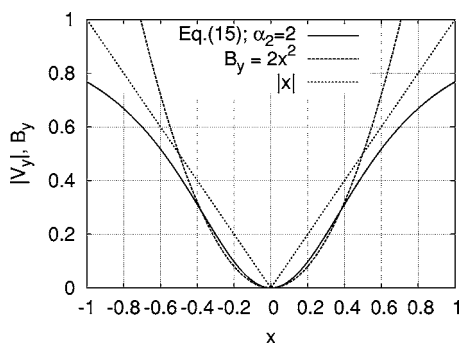


FIG. 4. Profile of the magnetic field and absolute value of the velocity.

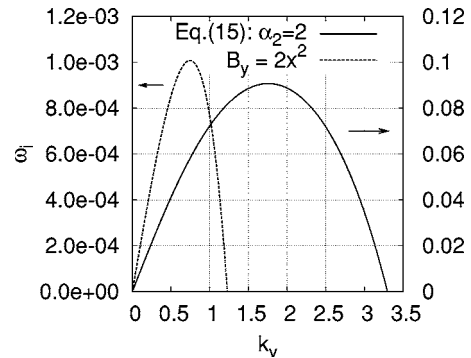


FIG. 5. Growth rate for the parabolic field profile and for (15). Notice that the scales of ordinates differ between two cases.

$|V_y(x)| = |x|$ . Note that the magnetic field at  $|x| \geq 0.4$  is weaker for the profile (15) than the parabolic one, while those in  $|x| \leq 0.4$  are very close to each other. The dispersion relations for these two cases are shown in Fig. 5. Notice that the scale of the ordinate for (15) is two orders of magnitude larger than that for the parabolic profile, and so as the maximum growth rate. The profile with weaker magnetic shear in the outer region yields a much larger growth rate than the parabolic case.

The reason becomes clear when we look at the eigenfunctions for  $k_y = 0.1$ ; see Fig. 6. As is seen from the figure, there are resonant and step-like structures around  $|x| \sim 0.5$  for the parabolic field profile, where  $|V_y| = B_y$ . Since the magnetic field is so strong that the local Alfvén velocity exceeds local flow velocity at  $|x| > 0.5$ , the eigenfunction cannot extend to the edge and is rather confined within  $|x| \leq 0.5$ . On the other hand, the Alfvén velocity corresponding to (15)

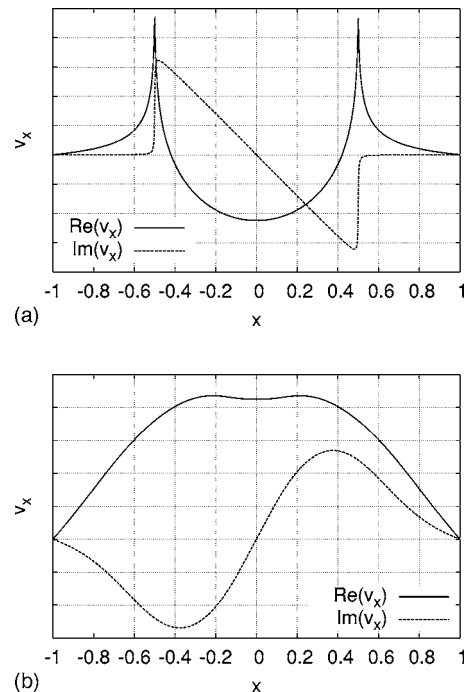


FIG. 6. Eigenfunctions (a) for parabolic profile and (b) for (15) with  $k_y = 0.1$ .

slower than the local flow velocity in the whole domain, therefore, the eigenfunction can be extended in the whole domain.

Thus we find that a strong magnetic field whose Alfvén velocity exceeds local flow velocity has a stabilizing effect on the mode. It is interesting to compare this result with the case with an interchange-type drive.<sup>7</sup> In Ref. 7, the shear flow stretching effect exhibited a stabilizing effect only when the flow velocity exceeded the Alfvén velocity. In the present example, this is analogous to the finding that there is a minimum on the magnetic field strength below which the instability is quenched (see Fig. 1). On the other hand, if the magnetic field is too strong compared to the flow velocity, the interchange-type instability was stabilized, which was expressed as the destabilizing effect of the shear flow in Ref. 7 from the opposite viewpoint. In the present case, this may correspond to the stabilizing effect of the edge magnetic shear in the parabolic field profile. The important point is that when the effects of field and flow are comparable, the maximum growth rate is achieved.

### 3. Larger growth rate

To reach nonlinear saturation, the growth must occur considerably faster than the decay of the background field, since inhomogeneity of the magnetic field is one of the source for the instability. For this purpose, we may point out two effects that increase the growth rate, according to the results obtained from previous two subsections: (1) to make the central  $B_y$  value negative, and (2) to make the edge magnetic shear weak. Paying attention to these facts, we prepared a profile

$$B_y(x) = \frac{1}{2}(x^2 + 1) - \frac{1}{\cosh^2(2x)} - \frac{\alpha_3}{\beta_3}[e^{\beta_3(x-1)} + e^{-\beta_3(x+1)}], \quad (16)$$

where  $\alpha_3$  and  $\beta_3$  are introduced so that the current density vanishes at the edge, which is needed for the following resistive simulation. Here we take  $\alpha_3 \approx 1.27$  and  $\beta_3 = 10$ . Profile (16) is shown in Fig. 7 together with the flow profile for comparison, and the corresponding maximum growth rate is about  $\omega_i \approx 0.153$  for  $k_y \approx 1$ .

### B. Application to tokamak $q_{\min}$ surface

When the velocity is everywhere parallel to magnetic field (as discussed in the previous section), the mass velocity must be comparable to the Alfvén velocity for the instability to occur. However, by adding a perpendicular field, we may reduce the velocity required for instability to be much smaller than both of parallel and perpendicular components of the field. Here we here show an example of the tokamak  $q_{\min}$  surface in slab geometry.

Let us assume a parabolic safety factor profile:

$$q = x^2 + q_{\min} \left( = \frac{aB_T}{RB_p} \right), \quad (17)$$

with

$$R/a = 3, \quad q_{\min} = 1.7, \quad (18)$$

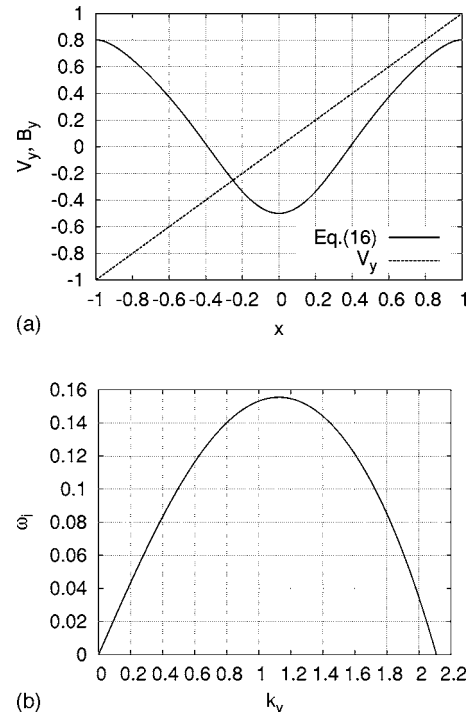


FIG. 7. Profile (16) that makes the growth rate larger, and the corresponding dispersion relation.

$$(m, n) = (2, 1), \quad k_y = 1, \quad (19)$$

$$B_z = 5.0, \quad (20)$$

where  $R$  and  $a$  denote the major and minor radius, respectively; then

$$V_y = \sigma x \quad (21)$$

would yield an instability with a growth rate  $\max_{\sigma} \omega_i \approx 0.016$  for  $\sigma \approx 0.23$ . In this example, the instability is observed for  $0.18 \lesssim \sigma \lesssim 0.3$ . Notice that the growth rate  $\omega_i$  is one order of magnitude smaller than the flow shear  $\sigma$ , which is significantly smaller even than the poloidal Alfvén velocity.

Figure 8 shows the profile and eigenfunction obtained from the shooting code for  $\sigma = 0.23$ . As is clearly seen in Fig. 8, the velocity is everywhere smaller than both the local poloidal ( $y$  component) and toroidal ( $z$  component) field, however,  $|\mathbf{k} \cdot \mathbf{V}|$  and  $|\mathbf{k} \cdot \mathbf{B}|$  have a similar magnitude and the sufficient condition (12) is violated. A somewhat peaked structure is observed in the eigenfunction around  $x \approx \pm 0.4$ , corresponding to the resonant radius where  $|\mathbf{k} \cdot \mathbf{V}| \approx |\mathbf{k} \cdot \mathbf{B}|$ . The important point is that, as far as the slab model is concerned, the instability can take place if the *difference* of flow is comparable to the *difference* of poloidal Alfvén velocity in the region of the sheared velocity.

The sufficient condition for stability given by (12) takes a simple form when we restrict ourselves to a linear shear flow and symmetric parabolic field profiles, respectively,

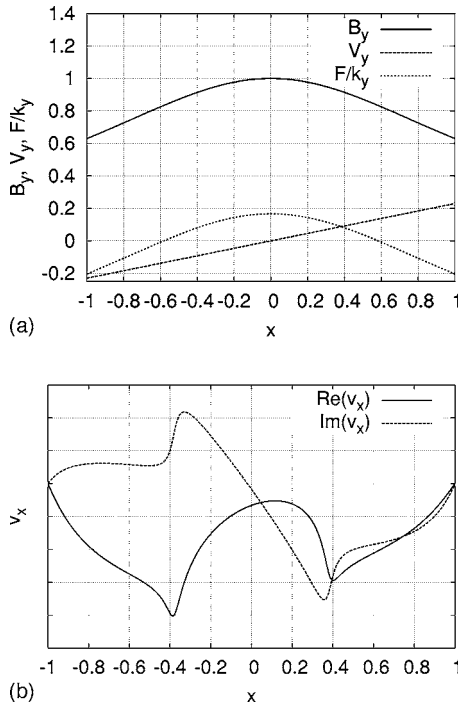


FIG. 8. Background field and velocity profile and eigenfunction  $v_x$  corresponding to  $k_y=1$ .

$$V_y'^2 < 4B_y''(0) \left( B_y(0) + \frac{k_z}{k_y} B_z \right), \quad (22)$$

which in turn yields the following stability condition in the physical units:

$$\left( \frac{dV_y}{dx} \right)^2 < 4v_{pA}^2 \frac{d^2q}{dx^2} \left( \frac{n}{m} - \frac{1}{q_{\min}} \right), \quad (23)$$

where  $v_{pA}^2 = B_y^2(0) / \mu_0 \rho$  is the local poloidal Alfvén velocity, and we assumed a uniform toroidal field.

We must address two cautions on the stability condition (23). First, (23) is formulated as a local condition under the assumption of linear flow and symmetric parabolic field profiles, while this instability is essentially a global one. Since the smaller magnetic shear in the edge region brought about larger growth rate as we saw in Sec. III, a more realistic field profile might make the equilibrium more unstable than evaluated from this model. Second, it is derived from the sufficient condition for stability. It is clear that whenever  $q$  crosses a rational number [or  $(nq_{\min} - m)$  becomes negative], the condition (23) is violated, however, there are many stable examples that may violate (23), even for the symmetric parabolic field profile (note the lower limit of  $B_y''$  obtained by Chen and Morrison<sup>5</sup>). Besides, one has to restrict the application to a low  $m/n$  mode since this instability does not arise for a too large  $k_y$ . Nevertheless, this condition may be useful to get a rough idea on the regime of the instability. If  $V_y'$  is far smaller than the right-hand side, then the equilibrium may be stable for this instability, but if they are comparable, one may have to check the stability numerically for that specific profiles.

## IV. NUMERICAL SIMULATION

In order to investigate the nonlinear behavior of the instability, we have developed a two-dimensional pseudospectral reduced MHD code, which solves

$$\partial_t \Delta \phi + \{ \phi, \Delta \phi \} - \{ \psi, \Delta \psi \} = \nu \Delta^2 \phi, \quad (24)$$

$$\partial_t \psi + \{ \phi, \psi \} = \eta \Delta \psi, \quad (25)$$

where  $\{P, Q\} = (\partial_y P)(\partial_x Q) - (\partial_x P)(\partial_y Q)$  is the standard Poisson bracket,  $\nu$  and  $\eta$  are (normalized) viscosity and resistivity, and  $\phi$  and  $\psi$  are the streamfunction and flux function, related to vector fields as

$$\mathbf{v} = \nabla \phi \times \mathbf{e}_z, \quad \mathbf{B} = \nabla \psi \times \mathbf{e}_z, \quad (26)$$

respectively. We impose no-slip and perfectly conducting boundary conditions on  $x = \pm 1$ , namely,

$$v_x = 0, \quad v_y = \text{const}, \quad B_x = 0, \quad j_z = 0, \quad (27)$$

and periodicity in the  $y$  direction. Note that we cannot use free-slip ( $\Delta \phi = 0$ ) boundary condition in order to sustain linear profile of the background shear flow. In principle, finite resistivity introduces the possibility of a tearing mode instability. We have carefully checked that the observed growth rate and nonlinear evolution show no correspondence to tearing mode physics (see later).

For tokamak applications, this code can make single-helicity calculation of Strauss' reduced MHD equations,<sup>17</sup>

$$\partial_t \nabla_{\perp}^2 U + \mathbf{v} \cdot \nabla \nabla_{\perp}^2 U = \mathbf{B} \cdot \nabla \nabla_{\perp}^2 A + \nu \nabla_{\perp}^2 \nabla_{\perp}^2 U, \quad (28)$$

$$\partial_t A = \mathbf{B} \cdot \nabla U + \eta \nabla_{\perp}^2 A, \quad (29)$$

by changing the definition of the Laplacian, Poisson bracket, and flux function to

$$\nabla_{\perp}^2 = \partial_x^2 + \partial_{\zeta}^2, \quad (30)$$

$$\{P, Q\} = \partial_{\zeta} P \partial_x Q - \partial_x P \partial_{\zeta} Q, \quad (31)$$

$$\psi = A - \alpha B_z x, \quad (32)$$

$$\phi = U, \quad (33)$$

where  $\zeta = y + \alpha z$  is the helical coordinate.<sup>18</sup> The single-helicity calculation may be justified because there is only a single set of unstable low wavenumbers in the example shown later. The inclusion of another dimension should not significantly alter the results.

### A. Numerical scheme

In order to impose nonperiodic boundary conditions in the  $x$  direction, we used Chebyshev polynomials as basis functions. This admits the use of the fast Fourier transform due to the property

$$T_n(\cos \theta) = \cos(n\theta), \quad (34)$$

where  $T_n$  is the  $n$ th order Chebyshev polynomial. It is noted that Chebyshev polynomial expansion has an exponential convergence for any smooth function defined on a finite non-periodic domain while the Fourier is algebraic in this case.<sup>19</sup>

We use Orszag's two-thirds rule<sup>20</sup> to remove the aliasing effect from nonlinear terms. One disadvantage of using Chebyshev polynomials may be the accumulation of the round-off errors in calculating derivatives,<sup>21</sup> however, this should not invalidate our calculation in the range of mode numbers we take in our calculations ( $2N/3 \leq 1152$ , where  $N+1$  is the number of grid points in  $x$ ). The periodic direction ( $y$ ) is expanded by the Fourier series, as usual.

Time integration is conducted by the third-order Adams-Bashforth scheme for nonlinear terms and the Crank-Nicholson scheme for dissipative ones.<sup>22</sup> The time step is chosen at each step so that it avoids numerical instability. See Sec. A 1 for the AB3 formula for an uneven time step. The reason we used a different scheme depending on linear/nonlinear terms is basically because of the numerical stability. The dissipative terms bring the highest order restrictions on time steps in connection with the spatial grid, which is of  $O(\Delta x^2)$ , where  $\Delta x$  is the smallest grid size. In the Chebyshev pseudospectral scheme, we use the Chebyshev-Lobatto (extrema) grid, which is concentrated at the edge as  $\Delta x \sim O(1/N^2)$ . Thus the time step allowed by an explicit scheme would be extremely small [of the order  $O(1/N^4)$ ], which is impractical. On the other hand, using the Crank-Nicholson scheme for nonlinear terms is not simple since one needs to solve the nonlinear boundary value problem at each time step, which would require iteration of the matrix inversion.

The boundary conditions written in (27) are on velocity and magnetic fields for which we are not directly solving equations. Equations (24) and (25) demand two boundary conditions on vorticity  $\Delta\phi$  and flux function  $\psi$  at each time step, and two on streamfunction  $\phi$  when solving the Poisson equation. By converting the  $v_y$  condition with the method of Coutsias *et al.*,<sup>23</sup> we imposed, in the  $n$ th Fourier space,

$$\phi_n = 0, \quad (35)$$

$$\sum_m B_{mn}(\Delta\phi)_{mn} = 0, \quad (36)$$

at  $x = \pm 1$  for  $k_y \neq 0$  ( $n \neq 0$ ), and

$$\partial_x \phi_0 = \text{const} \quad \text{at} \quad x = 1, \quad (37)$$

$$\partial_x(\Delta\phi)_0 = 0 \quad \text{at} \quad x = \pm 1, \quad (38)$$

for  $k_y = 0$  ( $n = 0$ ), where  $(\Delta\phi)_{mn}$  denotes the  $m$ th Chebyshev and  $n$ th Fourier amplitude of the vorticity and  $B_{mn}$  denotes the numerical matrix described in Ref. 23. The arbitrariness of constant for the potential  $\phi$  is determined by  $\phi_{00} = 0$ . The boundary condition on magnetic field (and current density) is readily converted to the one on  $\psi$ :

$$\psi = \text{const} \quad (\text{in time and along each wall}). \quad (39)$$

We use a preconditioner for the inversion of the matrices in solving Poisson equation and Crank-Nicholson time stepping, as introduced by Coutsias *et al.*<sup>24</sup> Since the derivative matrix for Chebyshev polynomials is upper-triangular, the simple inversion of the Laplacian needs  $O(N^2)$  operation for

each  $k_y$ . On the other hand the integral operation is described by the band-diagonal matrix due to the three-term recursion relation:

$$\int T_n(x) dx = \frac{T_{n+1}(x)}{2(n+1)} - \frac{T_{n-1}(x)}{2(n-1)} + C(n \geq 2). \quad (40)$$

Thus, by multiplying the integral matrix prior to inversion, one may carry out all matrix inversions by  $O(N)$  operations for each  $k_y$ . A more detailed description is given in Sec. A 2. Boundary conditions are imposed by the Sherman-Morrison formula.<sup>25</sup>

As is often referred in spectral simulations, the Fourier-Chebyshev amplitude corresponding to the highest wavenumber component may be regarded as an empirical measure of the numerical error. Using this fact, we may automatically control the resolution, which greatly enhances the performance in linear instability and/or decaying turbulence simulations. The code checks the ratio between the amplitude of the largest wavenumber component and that of the largest component of the vorticity in the Fourier-Chebyshev space. When it becomes larger than  $u_{\text{lim}}$  (smaller than  $l_{\text{lim}}$ ), the resolution is enhanced (reduced). We have made these values adjustable, and the resolution of exact power of 2 is automatically assigned, while other mixed-radix grid points are given as inputs.

## B. Linear instability and its quasilinear effect

We first show the linear instability of the profiles:

$$V_y(x) = x, \quad (41)$$

$$B_y(x) = \frac{1}{2}(x^2 + 1) - \frac{1}{\cosh^2(2x)} - \frac{\alpha_3}{\beta_3} [e^{\beta_3(x-1)} + e^{-\beta_3(x+1)}], \quad (42)$$

which was introduced in Sec. III A 3. As we discussed before, this particular magnetic field profile was chosen to maximize the growth rate large, since this instability has a relatively small intrinsic growth rate. The parameters  $\alpha_3$  and  $\beta_3$  are introduced in order for the current density to vanish at the edge, and  $\alpha_3 \approx 1.27$  and  $\beta_3 = 10$  in the current run, respectively. We take  $L_y = 2\pi$  since  $k_y \approx 1$  gives the largest growth rate  $\omega_i \approx 0.153$  in this case.

Figure 9 shows the time evolution of the  $L^2$  norm of perturbed streamfunction  $\|\phi_1\|$ , enstrophy, and total energy when we put the initial perturbation of the form

$$(\Delta\phi)_1 = \frac{10^{-2}}{\cosh^2(10x)} \sin\left(\frac{2\pi(x+y)}{L_y}\right), \quad (43)$$

with various diffusivity, where the subscript 1 denotes the perturbed quantity. The enstrophy and energy are normalized by their initial values. The maximum numbers of grid points used in these simulations are summarized in Table I for a sufficient convergence. The number of grid points drastically increases as  $\nu = \eta$  becomes smaller than  $3 \times 10^{-4}$ , which suggests a qualitative difference between case (a)  $\nu = \eta \leq 2 \times 10^{-4}$  and case (b)  $\nu = \eta \geq 3 \times 10^{-4}$ . Figure 9 also shows a critical difference between cases (a) and (b): The  $\|\phi_1\|$  plot

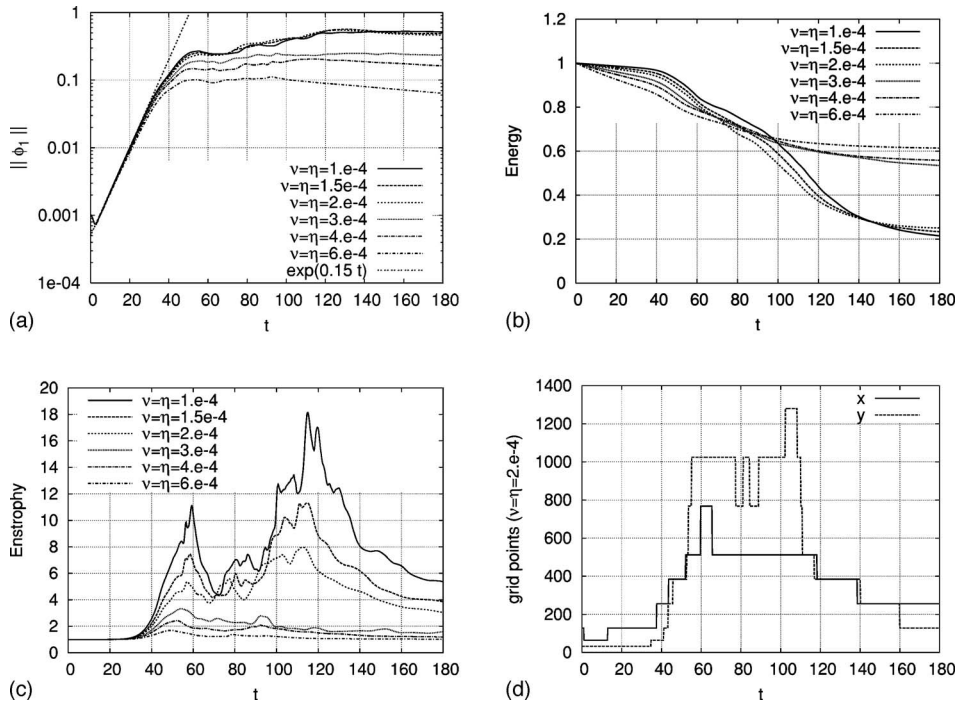


FIG. 9. Time evolutions of  $\|\phi_1\|$ , enstrophy, and total energy in the simulations with various diffusivity and number of grid points for the case with  $\nu = \eta = 2 \times 10^{-4}$ .

almost overlaps and the enstrophy increases drastically after  $t \geq 80$  for (a), and the energy dissipation rate jumps between (a) and (b) after  $t \geq 100$ . Case (b) is thought to be dissipation dominated, and the nonlinear evolution of the instability does not show interesting behavior. However, as diffusivity goes smaller, the nonlinear behavior becomes turbulent, and the flux surface is completely broken in a wide region. In this and subsequent sections, we focus on the case with  $\nu = \eta = 2 \times 10^{-4}$  since other simulations in case (a) show qualitatively similar behavior.

The straight line in the evolution of  $\|\phi_1\|$  shows the exponential growth, with growth rate 0.15. We notice that the growth rate of the simulation agrees well with that obtained from the shooting code, and it approaches the ideal value 0.153 (for  $\nu = \eta = 0$ ) as the dissipation rate becomes smaller.

Since the nonlinear evolution of the instability leads to a decaying turbulence simulation, it is necessary to consider the diffusion rate of the background field. It is governed by the decay of the eigenfunction of  $\partial_x^2$  with the smallest wavenumber. Currently we have a diffusion equation for  $\psi$ , which is an odd function, under the fixed boundary condition. Thus the smallest wavenumber eigenfunction corresponding to the profile (42) is  $\sin(\pi x)$  since  $L_x = 2$ , which in this case gives

TABLE I. Maximum numbers of grid points in the simulations.

case	$\nu = \eta$	Grids ( $x \times y$ )	$u_{\text{lim}}$
(a)	1.e-4	1728 $\times$ 4096	5.e-6
	1.5e-4	1024 $\times$ 2304	1.e-5
	2.e-4	768 $\times$ 1280	1.e-4
(b)	3.e-4	384 $\times$ 384	1.e-3
	4.e-4	256 $\times$ 256	1.e-3
	6.e-4	128 $\times$ 128	1.e-3

rise to the decay rate of the magnetic field of  $\pi^2 \eta$ . The  $e$ -fold time of the background magnetic field is, thus, estimated about  $t \sim 500$  for  $\eta = 2 \times 10^{-4}$ , and by that time, the instability will completely lose its drive by the diffusion of the background magnetic field.

Let us see the quasilinear effect of the instability. It is obtained by substituting linear eigenmode into nonlinear terms and by calculating its backreaction on the background field. Here we will work on the original vector form equation in order to see the effect on  $v_y$  and  $B_y$ :

$$\partial_t \mathbf{v}_0 = -(\mathbf{v}_1 \cdot \nabla \mathbf{v}_1)_0 + [(\nabla \times \mathbf{B}_1) \times \mathbf{B}_1]_0, \quad (44)$$

$$\partial_t \mathbf{B}_0 = [\nabla \times (\mathbf{v}_1 \times \mathbf{B}_1)]_0, \quad (45)$$

where the subscripts 0 and 1 denote the background ( $k_y = 0$ ) and linearly unstable ( $k_y = 1$ ) components of the fields, respectively.

By substituting

$$\mathbf{v}_1 = \nabla \tilde{\phi} \times \mathbf{e}_z, \quad \mathbf{B}_1 = \nabla \tilde{\psi} \times \mathbf{e}_z, \quad (46)$$

$$\tilde{\phi} = \tilde{\phi}_r \cos(k_y y) - \tilde{\phi}_i \sin(k_y y), \quad (47)$$

$$\tilde{\psi} = \tilde{\psi}_r \cos(k_y y) - \tilde{\psi}_i \sin(k_y y),$$

into (44) and (45) and taking the  $k_y = 0$  component of the rhs, we obtain

$$(\mathbf{v}_1 \cdot \nabla v_{1y})_0 = -\frac{k_y}{2} (\tilde{\phi}_r \partial_x^2 \tilde{\phi}_i - \tilde{\phi}_i \partial_x^2 \tilde{\phi}_r), \quad (48)$$

$$(\mathbf{B}_1 \cdot \nabla B_{1y})_0 = -\frac{k_y}{2} (\tilde{\psi}_r \partial_x^2 \tilde{\psi}_i - \tilde{\psi}_i \partial_x^2 \tilde{\psi}_r), \quad (49)$$

since

$$[(\nabla \times \mathbf{B}_1) \times \mathbf{B}_1]_0 = -\frac{1}{2}[\nabla(B_1^2)]_0 + (\mathbf{B}_1 \cdot \nabla \mathbf{B}_1)_0, \quad (50)$$

and the gradient term gives rise to no contribution on the evolution of the  $y$ -component field the same as the  $\nabla p$  term ( $k_y=0$ ). By making the same manipulation on the rhs of (45), we obtain

$$[\nabla \times (\mathbf{v}_1 \times \mathbf{B}_1)]_{0y} = \frac{k_y}{2} \partial_x^2 (\tilde{\phi}_r \tilde{\psi}_i - \tilde{\phi}_i \tilde{\psi}_r). \quad (51)$$

Since the linear eigenfunction is growing with the growth rate  $\omega_i$ , the evolution equations (44) and (45) yield

$$\partial_t v_{0y} = C e^{2\omega_i t} (\tilde{\phi}_r \partial_x^2 \tilde{\phi}_i - \tilde{\phi}_i \partial_x^2 \tilde{\phi}_r - \tilde{\psi}_r \partial_x^2 \tilde{\psi}_i + \tilde{\psi}_i \partial_x^2 \tilde{\psi}_r), \quad (52)$$

$$\partial_t B_{0y} = C e^{2\omega_i t} \partial_x^2 (\tilde{\phi}_r \tilde{\psi}_i - \tilde{\phi}_i \tilde{\psi}_r), \quad (53)$$

where  $C$  is a constant proportional to the square of the initial amplitude of the eigenmode. Note that temporal oscillation of the eigenfunction (if there is any) cancels out during the cancellation of  $k_y y$ .

Figure 10(a) is a plot of the rhs of (52) and (53), obtained from the numerical eigenfunction by means of the shooting method. We take 401 evenly spaced grid points and derivatives are calculated by means of the second order centered finite difference formula. Figure 10(b) shows the difference between the initial fields and solutions of nonlinear ideal ( $\nu = \eta = 0$ ) simulation at  $t=25$ , where  $k_y > 1$  components are artificially killed during evolution. The difference from (a) thus comes from the stable  $k_y=1$  oscillation that is excited initially and the self-consistent change of the eigenfunction due to the change of the background field. These two figures almost overlap with each other. Figure 10(c) shows the difference between solutions of full nonlinear simulation and that of the one-dimensional (1-D) linear diffusion equation for  $\psi$  (with the same  $\eta$  and grid points) at  $t=25$ , which includes the effect of dissipation on linear instability and all of the nonlinear effect including the backreaction from higher harmonics. The peaks are broadened somewhat due to the effect of dissipation but the qualitative agreement is good.

Here,  $B_y=0$  initially takes place around  $x \sim \pm 0.39$ . We can see that the quasilinear effect of the instability on the equilibrium affects the velocity and magnetic fields roughly equally. The energy ratio of the quasilinear magnetic/kinetic field modification is about 1.22 for the shooting result. (It affects more on the magnetic field in the energy norm while the maximum is larger for the velocity in Fig. 10.) The velocity is flattened and magnetic field is weakened around the origin. As can be seen from the figure, most of the effect takes place where  $B_y < 0$ , and the area where  $B_y$  is negative is slowly widened because of the fact that  $\partial_t B_{0y} < 0$  at  $x \sim \pm 0.39$ . This is necessary to push up the central value of  $B_y$  since we are imposing the constraint that  $\int B_y dx = \text{const}$  by placing the ideally conducting wall.

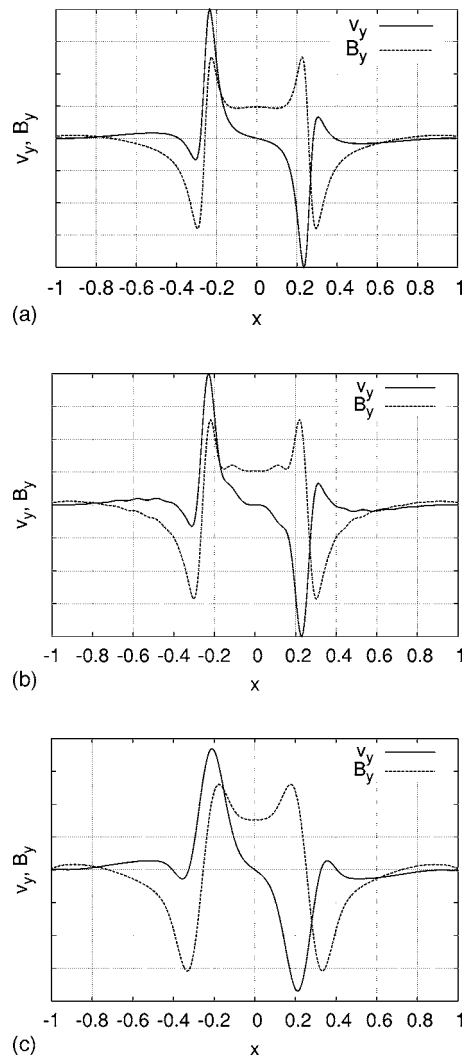


FIG. 10. Quasilinear effect of the instability: (a) evaluated from (52) and (53) with a shooting result, (b) at  $t=25$  in the ideal simulation with  $k_y > 1$  artificially killed, and (c) at  $t=25$  in the dissipative simulation with full nonlinearity.

### C. Nonlinear evolution

We now turn to the nonlinear effect of the instability. Time traces of the  $y$ -averaged velocity and magnetic fields are shown in Fig. 11. As is seen from the figure, the instability brings the positive  $B_y$  region just outside of  $B_y \sim 0$  to lower values, and at the same time it brings up the central  $B_y(0)$ , which was pointed out in the previous section. The instability does not alter the profile of velocity and field in the outer region  $|x| \gtrsim 0.6$ , and it flattens and makes them approach zero only in the central region. Note that the flattened flow profile looks as  $x^3$ , which is KH stable, albeit with an inflection point. The change of the  $B_y$  field at the edge is mostly attributed to the diffusion of the background magnetic field. According to an independent 1-D simulation of the linear diffusion equation for  $\psi$ , the edge discrepancy turned out to be within a few percent until  $t \leq 130$ .

The contour plots of streamfunction  $\phi$  and flux function  $\psi$  at  $t=45$  are shown in Fig. 12. Stretching and rolling up of the flux function is observed around two resonant surfaces,

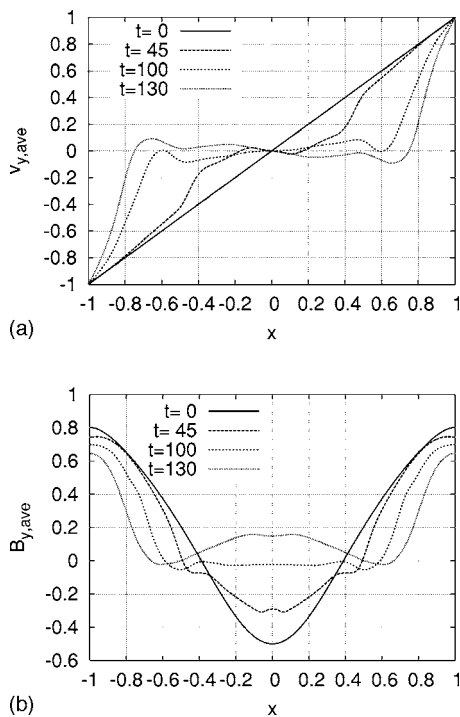
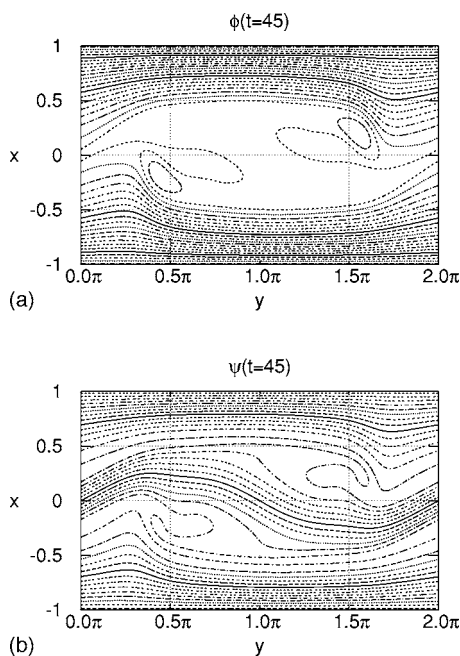
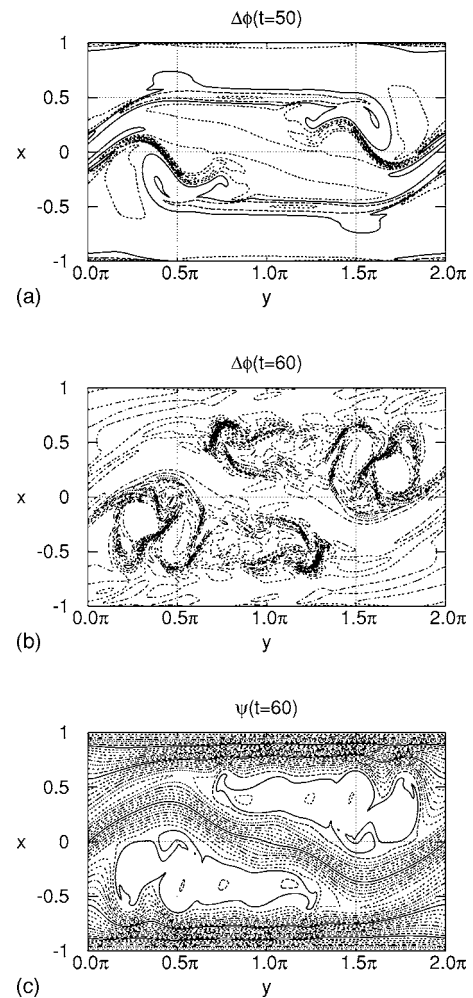


FIG. 11. Time evolution of the average flow and field.

qualitatively similar to a KH instability. The stage looks rather coherent and the effect of instability is restricted within  $|x| \lesssim 0.5$ .

By  $t \approx 50$ , the instability is strongly nonlinear. The size of the vortex keeps on growing and vorticity concentration is pushed outward yielding two high-vorticity lines around  $x \approx \pm 0.5$ . About the first maximum of the enstrophy ( $t \approx 57$ ), these two high vorticity lines are broken into vortex chains, as seen from Fig. 13. This stage from the first peak ( $t \approx 57$ )

FIG. 12. Contour plots of the streamfunction  $\phi$  and flux function  $\psi$  at  $t=45$ .FIG. 13. Contour plots of the vorticity at  $t=50$  and  $60$ , and the flux function at  $t=60$ .

to the second local minimum ( $t \approx 84$ ) of the enstrophy looks somewhat turbulent. At this stage, however, the turbulent structure is localized in two regions separated by a central magnetic field line. Reconnection takes place easily around each separated turbulent region since the equilibrium magnetic field line reverses along  $x \approx \pm 0.4$ . However, this is inhibited at the center.

After  $t \approx 60$ , the vortex chains start to merge in each region and try to entangle the central horizontal magnetic field line in a clockwise manner. The entanglement of the field line once reaches maximum around  $t \approx 75$ , and the field line reflects these vortex chains due to its tension force (see Fig. 14). The reflected vortices merge further in each region and form two large vortices of the same polarity. These two large vortices entangle the central field line again, and reconnection starts around top and bottom regions along  $y \approx \pi$ .

At  $t \approx 100$ , there are two large vortices with the same polarities (centered around  $y \sim 0.6\pi$  and  $1.4\pi$ ) and a small one with an opposite polarity (centered around  $y \sim 0$  or  $2\pi$ ); see Fig. 15. Because of the same polarity, a high-vorticity line is formed and squeezed between them as their sizes are getting large, which causes the increase of the resolution in the  $y$  direction (see Fig. 9). At this time, the  $\psi$  contour shows

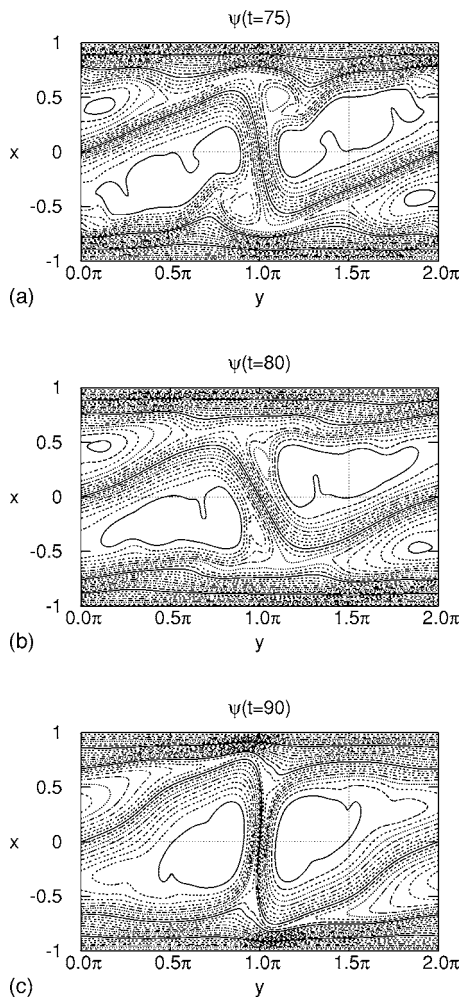


FIG. 14. Entanglement of the central field line.

two large islands extending to  $|x| \lesssim 0.8$ , indicating a large energy transport along the field line. Strong current sheets are observed along horizontal lines  $x \approx \pm 0.8$  and along a vertical line  $y \approx \pi$ . However, the two islands have the opposite polarity, and magnetic reconnection is mainly observed along horizontal current sheets. It is noted that the second reconnection event does not take place for smaller diffusivity [case (b)] so that the central field line separates the two turbulent regions all the time. However, the critical diffusivity needed for the reconnection of the central field line is a subtle issue depending on the amplitude of the initial perturbation, since the background field profile decays away before the appearance of a turbulent state when one puts a tiny perturbation in the initial condition. Recall that the decay time of the background field profile is about 500 for  $\eta = 2 \times 10^{-4}$ . The average velocity and magnetic field at  $t = 100$  is flattened in a fairly wide range of the domain, and is close to zero in  $|x| \lesssim 0.5$ .

At the final peak of the enstrophy ( $t \approx 113$ ), the high-vorticity line is broken at the center of the domain, and the two vortices start to merge. The enstrophy monotonically decreases while the large merged vortex absorbs the smaller one with the opposite polarity, and the weaker vortex remains at  $t = 180$ . The average  $B_y$  is further pushed upward,

and it becomes positive almost everywhere in the domain by  $t = 130$ . The average flow is also flattened in a wider region.

We may apply this result to the tokamak  $q_{\min}$  surface.<sup>18</sup> In this case, the two-dimensional simulation is regarded as a single helicity calculation, and  $B_y = 0$  corresponds to the resonant surface of the corresponding mode. Since the tokamak has a strong toroidal field, it is convenient to consider a normalization to the velocity. In this case, the  $B_y^*$  used for the normalization in Sec. II is regarded as a value whose corresponding Alfvén velocity gives a comparable magnitude of the surrounding mass flow velocity. It may be significantly smaller than both the poloidal and toroidal fields.

Since the sign of  $B_y$  does not matter on the results of the instability, we may regard the minimum of  $B_y$  as a  $q_{\min}$  surface by flipping the  $B_y$  profile. The change of the sign of  $B_y$  corresponds to the fact that  $q$  crosses a rational value for the mode we are interested in. The time evolution of the average field suggests that we may have some difficulty in making  $q$  cross the rational (or integral) value. Moreover, it may lead to a major (or minor) disruption according to the large scale rearrangement of  $v_y$  and  $B_y$  (Note that we are using no-slip and ideal-wall boundary conditions; the ideal wall implies that the spatial integral of average  $B_y$  has to be conserved, which is, in some sense, suppressing the instability.)

Of course, the occurrence of disruption should be tested in a larger simulation with a more realistic geometry (in this case flow profile may contain an inflection point). We can anticipate what should be observed from our analysis. The frequency of the instability is zero here since we assumed symmetry in the flow profile, but it may be finite if the flow profile is asymmetric. As is easily understood when one makes a Galilean transform so that central  $v_y$  is finite, there appears a finite frequency arising from the Doppler shift, and it is of the order of the background flow transit frequency. Because of the global structure of the instability, the fluctuation would appear in low mode numbers. The flux function will be stretched and rolled up around two rational surfaces, as is seen in Fig. 12. On the other hand, the diamagnetic effect might be able to stabilize it in the presence of the background pressure gradient as is the case of KH instability.<sup>2</sup>

## V. CONCLUSION

The linear instability incurred by shear flow without an inflection point is investigated in slab geometry by numerically solving linear eigenvalue equation and by performing a two-dimensional (or single-helicity) nonlinear simulation.

We fixed the shear flow profile with a spatially linear function, and mainly focused on the effect of various symmetric field profiles. From the investigation using the shooting code, the typical field profile that gives a large growth rate has a few features: (a) the phase velocity of the Alfvén wave *in the direction of* the background mass velocity in the outer region has comparable, but smaller, values than the local mass flow; (b) the central value of  $F (=k \cdot B)$  can be finite and has a different sign from both edges, and thus, (c)  $F$  changes sign twice in the domain. By adding a component in the field nonparallel to the flow, we also showed an ex-

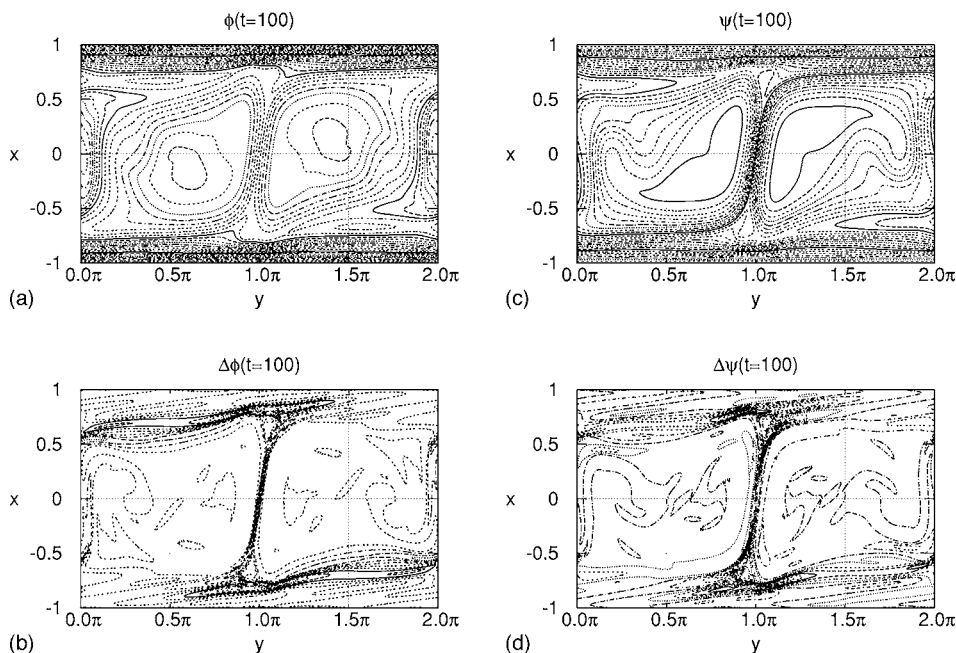


FIG. 15. Contour plots of the stream-function  $\phi$ , vorticity  $\Delta\phi$ , flux function  $\psi$ , and current density  $\Delta\psi$  at  $t=100$ .

ample that may be relevant to the  $q_{\min}$  surface of an advanced tokamak. Notice that (a) does not imply that mass velocity must exceed local Alfvén velocity. It can be significantly smaller than both toroidal and poloidal Alfvén velocity of a tokamak for the instability to occur.

In the numerical simulations, the growth rate is properly observed. The quasilinear effect of the instability is to push back the central value of the magnetic field in the direction where two zeros of  $F$  disappears, but the instability initially saturates before the central  $F$  changes sign. A weak turbulent state follows in the nonlinear stage, and after the sequence of vortex breakup/merges, background flow and field profiles are flattened in a fairly wide region. The negative region of  $F$  finally disappears due to their nonlinear interactions. The field line topology changes drastically, suggesting a huge energy transport across negative/positive regions of the magnetic shear, and the negative region of  $F$  finally disappears. When it is applied to the tokamak  $q_{\min}$  surface, the disappearance of the negative- $F$  region means the difficulty of  $q_{\min}$  crossing the integral (or rational) value, and the large scale rearrangement of  $v$  and  $B$  may imply the disruption.

To understand the role of this instability in tokamak disruptions, it would be necessary to consider more realistic geometry. There are effects that could significantly alter the growth rate and the threshold of the instability. First may be the existence of an inflection point, and others would include magnetic curvature and kinetic effects. One may obtain a more realistic condition of instability than (23) by adding more physics. However, the nonlinear evolution of the instability shown here would be valid once this instability takes place. As we have seen the breakup of the flux surface and flow profile in the nonlinear evolution, especially at the central region where the transport barrier is thought to be located, MHD instability may be considered a possible candidate of disruption when flow is included.

In the recent experiment in JT-60U, an intermediate time scale instability is observed in the reversed shear discharges,

which is too fast as a resistive instability, and too slow as an ideal one.<sup>9</sup> The instability reported in this paper is a good candidate for explaining these observations, as it evolves on the corresponding (intermediate) time scale. It is driven by the shear flow, and its characteristic growth time can even be one order of magnitude longer than the poloidal flow transit time. We have concentrated on the case without an inflection point to focus on the simplest dynamics of magneto-flow instability in this paper, however, it is also true for the case with the inflection point that the mass flow with neither of toroidal nor poloidal Alfvén velocity is needed for the instability. The inclusion of inflection point may make the equilibrium more unstable and the growth rate may increase accordingly, however, it is still true that the growth rate is governed by the flow, whose inverse is typically much slower than any Alfvén time. As the importance of shear flow effect on resistive instability is pointed out in Ref. 26, that in ideal MHD also needs to be investigated more thoroughly since a considerable amount of shear flow is expected in the advanced tokamak.<sup>11</sup> Moreover, it may also be applicable to instabilities observed in the tokamak edge, if the bootstrap and diamagnetic currents are strong enough to reverse the magnetic shear locally.

## ACKNOWLEDGMENTS

We acknowledge fruitful discussions with Dr. Zensho Yoshida, Dr. Greg Hammett, Dr. Frank Waelbroeck, and Dr. Swadesh Mahajan.

This research is in part supported by the U.S. DOE Center for Multiscale Plasma Dynamics. A part of the simulations are conducted at SX-7 in the National Institute for Fusion Sciences, Japan.

## APPENDIX: NUMERICAL ALGORITHM

### 1. AB3 formula for uneven time step

Let the differential equation be

$$\frac{\partial y}{\partial t} = f. \quad (\text{A1})$$

The Adams-Bashforth formula approximates the right-hand side by the polynomial  $\tilde{f}(t)$  from a finite number of sample points, and integrate the extrapolated polynomial to obtain  $y$  at the next step:

$$y^{(n+1)} = y^{(n)} + \int_{t^{(n)}}^{t^{(n+1)}} \tilde{f}(t) dt, \quad (\text{A2})$$

where the superscript ( $n$ ) denotes the  $n$ th time step. We may obtain it for the uneven time step by using Lagrangian polynomial for  $\tilde{f}(t)$ . Here we show the formula for the third order scheme, which uses a quadratic polynomial for  $\tilde{f}(t)$ :

$$\begin{aligned} \tilde{f}(t) = & \frac{(t-t^{(n-1)})(t-t^{(n-2)})}{\Delta_1(\Delta_1+\Delta_2)} f^{(n)} - \frac{(t-t^{(n)})(t-t^{(n-2)})}{\Delta_1\Delta_2} f^{(n-1)} \\ & + \frac{(t-t^{(n)})(t-t^{(n-1)})}{\Delta_2(\Delta_1+\Delta_2)} f^{(n-2)}, \end{aligned} \quad (\text{A3})$$

where we have defined

$$\Delta_0 = t^{(n+1)} - t^{(n)}, \quad \Delta_1 = t^{(n)} - t^{(n-1)}, \quad \Delta_2 = t^{(n-1)} - t^{(n-2)}. \quad (\text{A4})$$

Substituting (A3) into (A2) and performing the integration, we obtain

$$y^{(n+1)} = y^{(n)} + C_0 f^{(n)} + C_1 f^{(n-1)} + C_2 f^{(n-2)}, \quad (\text{A5})$$

where

$$\begin{aligned} C_0 = & \frac{1}{\Delta_1 + \Delta_2} \left[ \frac{(\Delta_0 + \Delta_1)^2}{\Delta_1} \left( \frac{\Delta_0 + \Delta_1}{3} + \frac{\Delta_2}{2} \right) \right. \\ & \left. - \Delta_1 \left( \frac{\Delta_1}{3} + \frac{\Delta_2}{2} \right) \right], \end{aligned} \quad (\text{A6})$$

$$C_1 = -\frac{\Delta_0^2}{\Delta_1\Delta_2} \left( \frac{\Delta_0}{3} + \frac{\Delta_1 + \Delta_2}{2} \right), \quad (\text{A7})$$

$$C_2 = \frac{\Delta_0^2}{\Delta_2(\Delta_1 + \Delta_2)} \left( \frac{\Delta_0}{3} + \frac{\Delta_1}{2} \right). \quad (\text{A8})$$

Of course, they converge to the normal AB3 coefficients for an even time step,

$$C_0 \rightarrow \frac{23}{12}\Delta, \quad C_1 \rightarrow -\frac{4}{3}\Delta, \quad C_2 \rightarrow \frac{5}{12}\Delta, \quad (\text{A9})$$

in the limit  $\Delta_{0,1,2} \rightarrow \Delta$ .

## 2. Preconditioner and time stepping

Let the Chebyshev expansion of a smooth function  $f(x)$  defined on  $x \in [-1, 1]$  and its first derivative  $f'(x)$  be

$$f(x) = \sum_l a_l T_l(x), \quad f'(x) = \sum_m b_m T_m(x). \quad (\text{A10})$$

Then the integral operation on Chebyshev amplitudes is expressed as

$$a_l = \sum_m \mathcal{D}_{lm}^{-1} b_m, \quad (\text{A11})$$

where  $\mathcal{D}^{-1}$  is a tridiagonal matrix defined from the integral three-term recursion relation (40):

$$\int T_j dx = \sum_i T_i \mathcal{D}_{ij}^{-1}. \quad (\text{A12})$$

The first row of  $\mathcal{D}^{-1}$  is arbitrary and is usually determined by the boundary condition. Here we define the matrix  $^{[1]}\mathcal{D}^{-1}$  in which the first row of  $\mathcal{D}^{-1}$  is replaced by zero. When we define  $\mathcal{D}$  by

$$b_l = \sum_m \mathcal{D}_{lm} a_m, \quad (\text{A13})$$

and  $^{[2]}\mathcal{D}^{-2} = ^{[2]}\mathcal{D}^{-1} (^{[1]}\mathcal{D}^{-1})^2$ , we find

$$^{[2]}\mathcal{D}^{-2} \mathcal{D}^2 = ^{[2]}\mathcal{I} (\neq \mathcal{D}^2 ^{[2]}\mathcal{D}^{-2}). \quad (\text{A14})$$

Since  $^{[1]}\mathcal{D}^{-1}$  is a tridiagonal matrix with all diagonal components zero,  $^{[2]}\mathcal{D}^{-2}$  has nonzero components only at diagonal and the second super-/subdiagonal components. Thus we may divide  $^{[2]}\mathcal{D}^{-2}$  into odd and even parts to make two tridiagonal matrices of half size. We also note that all boundary conditions used here can be divided into odd/even parts without loss of generality.

At each time stepping of the vorticity equation, we first have to find streamfunction  $\phi$  from vorticity  $\chi (= \Delta\phi$ ; note that the sign is flipped in the definition of  $\chi$ ) by solving the Poisson equation:

$$(\mathcal{D}^2 - k_{y,n}^2) \phi_n = \chi_n \quad (\text{A15})$$

for each Fourier mode  $n$  (in the  $y$  direction). Instead of inverting the upper-triangular matrix  $(\mathcal{D}^2 - k_{y,n}^2)$ , we multiply the second integral operator  $^{[2]}\mathcal{D}^{-2}$  on both sides and obtain

$$(^{[2]}\mathcal{I} - k_{y,n}^2 ^{[2]}\mathcal{D}^{-2}) \phi_n = ^{[2]}\mathcal{D}^{-2} \chi_n. \quad (\text{A16})$$

We may replace the first two rows of (A16) by two boundary conditions, divide it into odd/even parts, and invert the resulting operator on the left-hand side. All matrices appearing in (A16) are tridiagonal when divided into odd/even parts (plus one dense row corresponding to the boundary conditions), therefore, one can solve it by  $O(N)$  operations. Besides, the operator  $(^{[2]}\mathcal{I} - k_{y,n}^2 ^{[2]}\mathcal{D}^{-2})$  is much better conditioned than  $(\mathcal{D}^2 - k_{y,n}^2)$ : For details about the condition numbers, see Ref. 24.

The same preconditioner is used for Crank-Nicholson time integration. The reduced MHD equations (24) and (25) basically consist of two parts that are convective (nonlinear) terms described by the Poisson bracket and diffusive (linear) terms described by the Laplacian. They are symbolically written as

$$\frac{\partial y}{\partial t} = \mathcal{N}y + \mathcal{L}y, \quad (\text{A17})$$

where  $\mathcal{N}$  and  $\mathcal{L}$  denote nonlinear and linear terms, respectively; especially,  $\mathcal{L} \propto (\mathcal{D}^2 - k_{y,n}^2)$  for the  $n$ th Fourier mode. As is mentioned in Sec. IV A, we use Adams-Bashforth for nonlinear, and Crank-Nicholson for linear terms, so the discretization would yield

$$\left(1 - \frac{\Delta t}{2} \mathcal{L}\right) y^{(n+1)} = y^{(n)} + \int_{t^{(n)}}^{t^{(n+1)}} \widetilde{\mathcal{N}}y dt + \frac{\Delta t}{2} \mathcal{L}y^{(n)}, \quad (\text{A18})$$

where  $\widetilde{\mathcal{N}}y$  denotes the extrapolated polynomial described in the previous section. Instead of inverting the upper-triangular matrix  $(1 - \Delta t \mathcal{L}/2)$  on the left-hand side, we first multiply  ${}^{[2]}\mathcal{D}^{-2}$  on both sides from left and then only the band matrix remains to be inverted.

<sup>1</sup>J. W. S. Rayleigh, Proc. London Math. Soc. **9**, 57 (1880).

<sup>2</sup>B. N. Rogers and W. Dorland, Phys. Plasmas **12**, 062511 (2005).

<sup>3</sup>M. E. Stern, Phys. Fluids **6**, 636 (1963).

<sup>4</sup>A. Kent, Phys. Fluids **9**, 1286 (1966); J. Plasma Phys. **2**, 543 (1968).

<sup>5</sup>X. L. Chen and P. J. Morrison, Phys. Fluids B **3**, 863 (1991).

<sup>6</sup>E. P. Velikhov, Sov. Phys. JETP **36**, 995 (1959); S. Chandrasekhar, Proc.

Natl. Acad. Sci. U.S.A. **46**, 253 (1960); S. A. Balbus and J. F. Hawley, Astrophys. J. **376**, 214 (1991).

<sup>7</sup>T. Tatsuno, Z. Yoshida, and S. M. Mahajan, Phys. Plasmas **10**, 2278 (2003).

<sup>8</sup>P. A. Gilman and P. A. Fox, Astrophys. J. **484**, 439 (1997); **510**, 1018 (1999); **522**, 1167 (1999).

<sup>9</sup>S. Takeji, S. Tokuda, T. Fujita *et al.*, Nucl. Fusion **42**, 5 (2002).

<sup>10</sup>Y. Miura and the JT-60 Team, Phys. Plasmas **10**, 1809 (2003).

<sup>11</sup>Y. Sakamoto, T. Suzuki, S. Ide *et al.*, Nucl. Fusion **44**, 876 (2004).

<sup>12</sup>F. Volponi, Z. Yoshida, and T. Tatsuno, Phys. Plasmas **7**, 2314 (2000).

<sup>13</sup>T. Tatsuno, F. Volponi, and Z. Yoshida, Phys. Plasmas **8**, 399 (2001).

<sup>14</sup>A. Ito, Z. Yoshida, T. Tatsuno *et al.*, Phys. Plasmas **9**, 4856 (2002).

<sup>15</sup>A. Miura and P. L. Pritchett, J. Geophys. Res. **87**, 7431 (1982).

<sup>16</sup>Y. Y. Lau and C. S. Liu, Phys. Fluids **23**, 939 (1980).

<sup>17</sup>H. R. Strauss, Phys. Fluids **19**, 134 (1976).

<sup>18</sup>T. Tatsuno and W. Dorland, J. Plasma Fusion Res. **1**, 015 (2006).

<sup>19</sup>J. P. Boyd, *Chebyshev and Fourier Spectral Method* (Dover, New York, 2000).

<sup>20</sup>S. A. Orszag, J. Atmos. Sci. **28**, 1074 (1971).

<sup>21</sup>K. S. Breuer and R. M. Everson, J. Comput. Phys. **99**, 56 (1992).

<sup>22</sup>J. D. Hoffman, *Numerical Methods for Engineers and Scientists*, 2nd ed. (Marcel Dekker, New York, 2001).

<sup>23</sup>E. A. Coutsias and J. P. Lynov, Physica D **51**, 482 (1991).

<sup>24</sup>E. A. Coutsias, T. Hagstrom, J. S. Hesthaven *et al.*, Spec. Issue Houston J. Math., 1996, p. 21.

<sup>25</sup>W. H. Press, S. A. Teukolsky, W. T. Vetterling *et al.*, *Numerical Recipes* (Cambridge University Press, Cambridge, 1988).

<sup>26</sup>Y. Ishii, M. Azumi, and Y. Kishimoto, Phys. Rev. Lett. **89**, 205002 (2002).